EPJ Web of Conferences **3**, 06004 (2010)
DOI:10.1051/epjconf/20100306004

α clustering and superdeformation of ^{28}Si

Yasutaka Taniguchi[1,a], Yoshiko Kanada-En'yo[2], and Masaaki Kimura[3]

[1] RIKEN Nishina Center for Accelerator-Based Science, RIKEN, Wako 351-0198, Japan
[2] Yukawa Institute for Theoretical Physics, Kyoto University, Kyoto 606-8502, Japan
[3] Creative Research Initiative "Sousei," Hokkaido University, Sapporo 001-0021, Japan

Abstract. We have studied positive-parity states of ^{28}Si using antisymmetrized molecular dynamics and multi-configuration mixing with constrained variation. Applying constraints to the cluster distance and the quadrupole deformation of the variational calculation, we have obtained basis wave functions that have various structures such as α-^{24}Mg and ^{12}C-^{16}O cluster structures as well as deformed structures. Superposing those basis wave functions, we have obtained a oblate ground state band, a β vibration band, a normal-deformed prolate band, and a superdeformed band. It is found that the superdeformed bands contain large amounts of the α-^{24}Mg cluster components. The results also suggest the presence of two excited bands with the developed α-^{24}Mg cluster structure, where the inter-cluster motion and the ^{24}Mg-cluster deformation play important roles.

1 Introduction

Clustering plays critical roles in excited states of *p*-shell and very light *sd*-shell nuclei such as ^{16}O and ^{20}Ne[1,2]. In spite of the importance of clustering in the $A \lesssim 20$ region, its role in the $A \gtrsim 30$ region has not been studied enough. In such a heavier mass region, other effects such as deformations are considered to become more important than in a lighter mass region. Recently, based on AMD calculations, there has been discussion that both mean-field and cluster aspects play important roles in the excited states of ^{32}S, ^{40}Ca and ^{44}Ti[3–6].

To understand the mean-field and cluster aspects in the heavier system, ^{28}Si is an important case, because ^{28}Si has a rich variety of structures in its excited states from view points of both clustering and deformations. In the ground state band and the low-lying excited band, the coexistence of the prolate and the oblate deformation has been studied for quite some time. The ground state band is oblately deformed, while the excited band built on the 0^+_3 state at 6.69 MeV is considered to have prolate deformation (prolate ND)[7–10]. Among these states, the β vibration of the oblate deformed ground state band generates the band built on the 0^+_2 state at 4.98 MeV[9,10]. Furthermore, Kubono *et al.* have proposed a largely deformed band called the "excited prolate" band based on a ^{12}C(^{20}Ne, α) reaction[11–13]. This band assignment, however, is not confirmed yet, because intra-band electromagnetic transitions have not been observed.

In the highly excited states of ^{28}Si, the cluster aspects have been discussed. The excited states from $E_x = 18$ to 30 MeV, which have been observed by ^{24}Mg(^{6}Li, d), ^{24}Mg(α, α) and ^{24}Mg(α, γ) reactions are suggested as candidates for the rotational band members that have an α-^{24}Mg cluster structure[14,15], but a detailed theoretical study of α-^{24}Mg cluster states has not been done.

We aim in the present work to investigate the nature of excited states of ^{28}Si, focusing on clustering and deformations in a unified manner. Shape coexistence and β-vibration are studied, and those states are discussed in relation to α-^{24}Mg cluster components. We also discuss the possible existence of the superdeformation and developed α-^{24}Mg cluster states.

The present paper is organized as follows: In Sec. 2, the framework of deformed-basis AMD + MCM is explained briefly. Results of energy variation imposing two kinds of constraints and analysis of the obtained wave functions are presented in Sec. 3. In Sec. 4, results of MCM and structures of low-lying states are discussed. Clustering aspects are discussed in Sec. 5. Finally, we give a summary and conclusions in Sec. 6. Details of this work was reported in [16].

2 Framework

We have used the theoretical framework of deformed-basis AMD + MCM with constraints[17]. The details are presented in Refs. [3,18,19].

2.1 Wave Function and Hamiltonian

The deformed-basis AMD wave function is a Slater determinant of triaxially deformed Gaussian wave packets,

$$|\Phi_{\rm int}\rangle = \hat{\mathcal{A}}|\varphi_1,\ \varphi_2, \cdots, \varphi_A\rangle, \quad (1)$$

$$|\varphi_i\rangle = |\phi_i,\ \chi_i,\ \tau_i\rangle, \quad (2)$$

[a] e-mail: yasutaka@riken.jp

$$\langle \mathbf{r}|\phi_i\rangle = \prod_{\sigma=x,y,z}\left(\frac{2\nu_\sigma}{\pi}\right)^{\frac{1}{4}} \exp\left[-\nu_\sigma\left(r_\sigma - \frac{Z_{i\sigma}}{\sqrt{\nu_\sigma}}\right)^2\right], \tag{3}$$

$$|\chi_i\rangle = \alpha_i|\uparrow\rangle + \beta_i|\downarrow\rangle, \tag{4}$$

$$|\tau_i\rangle = |p\rangle \text{ or } |n\rangle. \tag{5}$$

Here, the complex parameters $\mathbf{Z}_i$, which represent the centroids of the Gaussian wave packets in phase space, take independent values for each single-particle wave function. The width parameters ν_x, ν_y, and ν_z are real parameters and take independent values for each of the x-, y- and z-directions, but are common for all nucleons. The spin part $|\chi_i\rangle$ is parameterized by α_i and β_i and the isospin part $|\tau_i\rangle$ is fixed as $|p\rangle$ (proton) or $|n\rangle$ (neutron). The values $\{\mathbf{Z}_i, \alpha_i, \beta_i\}$ $(i = 1, \cdots, A)$, ν_x, ν_y and ν_z are variational parameters and are optimized by energy variation as explained below.

The trial wave function in the energy variation with constraints is a parity-projected wave function,

$$|\Phi^\pi\rangle = \frac{1+\pi\hat{P}_r}{2}|\Phi_{\rm int}\rangle, \tag{6}$$

where π is parity and $\hat{P}_r$ is the parity operator. In this study, we will discuss positive-parity states.

The Hamiltonian is,

$$\hat{H} = \hat{K} + \hat{V}_{\rm N} + \hat{V}_{\rm C} - \hat{K}_{\rm G}, \tag{7}$$

where $\hat{K}$ and $\hat{K}_{\rm G}$ are the kinetic energy and the energy of the center of mass motion, respectively, and $\hat{V}_{\rm N}$ is the effective nucleon-nucleon interaction. We have used the Gogny D1S force[20].

2.2 Energy Variation

We have performed energy variation and optimized the variational parameters included in the trial wave function [Eqs. (1–5)] to find the state that minimizes the energy of the system E^π,

$$E^\pi = \frac{\langle\Phi^\pi|\hat{H}|\Phi^\pi\rangle}{\langle\Phi^\pi|\Phi^\pi\rangle} + V_{\rm cnst}. \tag{8}$$

Here, we add the constraint potential $V_{\rm cnst}$ to the expectation value of Hamiltonian $\hat{H}$ in order to obtain energy-minimum states under the optional constraint condition. In this study, we employ two types of constraints, one on the quadrupole deformation parameter β (β constraint) and other on the distance between clusters' centers of mass d (d constraint) by using the potential $V_{\rm cnst}$,

$$V_{\rm cnst} = \begin{cases} v^\beta_{\rm cnst}(\beta-\tilde{\beta})^2 & \text{for } \beta \text{ constraint,} \\ v^d_{\rm cnst}(d_{\rm C_m\text{-}C_n} - \tilde{d}_{\rm C_m\text{-}C_n})^2 & \text{for } d \text{ constraint.} \end{cases}. \tag{9}$$

Here β is the matter quadrupole deformation parameter, and $d_{\rm C_m\text{-}C_n}$ is the distance between the clusters' centers of mass $\rm C_m$ and $\rm C_n$,

$$d_{\rm C_m\text{-}C_n} = \left|\mathbf{R}_{\rm C_m\text{-}C_n}\right|, \tag{10}$$

$$\mathbf{R}_{\rm C_m\text{-}C_n} = \mathbf{R}_{\rm C_m} - \mathbf{R}_{\rm C_n}, \tag{11}$$

$$R_{{\rm C}_n\sigma} = \frac{1}{A_{\rm C_n}}\sum_{i\in {\rm C}_n}\frac{{\rm Re}Z_{i\sigma}}{\sqrt{\nu_\sigma}}, \tag{12}$$

where $A_{\rm C_n}$ is the mass number of cluster $\rm C_n$ and the expression $i \in {\rm C}_n$ means that the ith nucleon is contained in cluster $\rm C_n$. It should be noted that the σ $(= x, y, z)$ component of the spatial center of the single-particle wave function $|\varphi_i\rangle$ is $\frac{{\rm Re}Z_{i\sigma}}{\sqrt{\nu_\sigma}}$. When sufficiently large values are chosen for $v^\beta_{\rm cnst}$ and $v^d_{\rm cnst}$, the resultant values β and $d_{\rm C_m\text{-}C_n}$ of energy variation become $\tilde{\beta}$ and $\tilde{d}_{\rm C_m\text{-}C_n}$, respectively. We constrain the $d_{\alpha\text{-}^{24}{\rm Mg}}$ and $d_{^{12}{\rm C}\text{-}^{16}{\rm O}}$ values for the d constraint. In each calculation of energy variation, we constrain one of the values β, $d_{\alpha\text{-}^{24}{\rm Mg}}$ and $d_{^{12}{\rm C}\text{-}^{16}{\rm O}}$. Other quantities such as triaxiality γ are not constrained and optimized by the energy variation.

The energy variation with the AMD wave function is carried out using the frictional cooling method[21]. The time evolution equation for the complex parameters $\mathbf{Z}_i, \alpha_i$ and β_i is

$$\frac{dX_i}{dt} = -\mu_X\frac{\partial E^\pi}{\partial X_i^*}, \ (i = 1, 2, \cdots, A), \tag{13}$$

where X_i is $\mathbf{Z}_i, \alpha_i$ or β_i, and the time evolution equation for the real parameters ν_x, ν_y, and ν_z is

$$\frac{d\nu_\sigma}{dt} = -\mu_\nu\frac{\partial E^\pi}{\partial \nu_\sigma}, \ (\sigma = x, y, z). \tag{14}$$

The quantities μ_X and μ_ν are arbitrary positive real numbers. The energy of the system decreases as time progresses, and after a sufficient number of time steps, we obtain a minimum energy state under the condition satisfying the given constraint.

2.3 Angular Momentum Projection and Multi-conf guration Mixing

After performing the constraint energy variation for $|\Phi^\pi\rangle$, we superpose the optimized wave functions by employing the quadrupole deformation parameter β and the distances between the centers of mass among clusters $d_{\rm C_m\text{-}C_n}$ for the $\rm C_m$-$\rm C_n$ configurations,

$$|\Phi^{J^\pi}_M\rangle = \sum_K \hat{P}^{J^\pi}_{MK}\left(\sum_i f^\beta_{iK}|\Phi^\beta_i\rangle + \sum_{i,{\rm C_m\text{-}C_n}} f^{d_{\rm C_m\text{-}C_n}}_{iK}|\Phi^{d_{\rm C_m\text{-}C_n}}_i\rangle\right) \tag{15}$$

where $\hat{P}^{J^\pi}_{MK}$ is the parity and total angular momentum projection operator, and $|\Phi^\beta_i\rangle$ and $|\Phi^{d_{\rm C_m\text{-}C_n}}_i\rangle$ are optimized wave functions with β and $d_{\rm C_m\text{-}C_n}$ constraints for the constrained values $\tilde{\beta}^{(i)}$ and $\tilde{d}^{(i)}_{\rm C_m\text{-}C_n}$ respectively. The integrals over the three Euler angles in the total angular momentum projection operator $\hat{P}^J_{MK}$ are evaluated by numerical integration. The mesh widths in numerical integration are $2\pi/9, \pi/257$ and $2\pi/9$ for α, β and γ, respectively. Here the body-fixed x-, y- and z-axis are chosen as $\langle x^2\rangle \le \langle y^2\rangle \le \langle z^2\rangle$ for $\gamma < 30^\circ$ wave functions and $\langle x^2\rangle \ge \langle y^2\rangle \ge \langle z^2\rangle$ for $\gamma > 30^\circ$ ones in the case of β constrained wave functions. In the

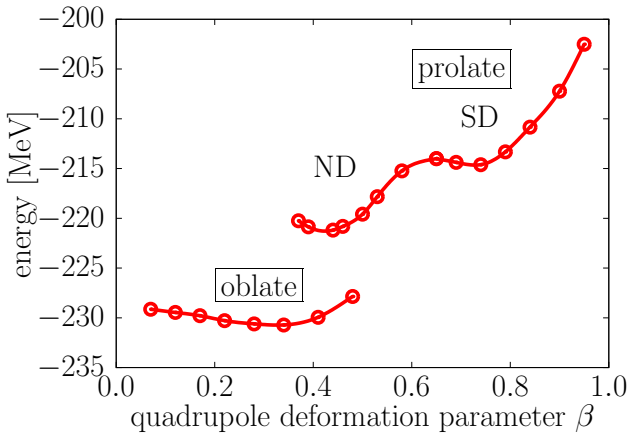

Fig. 1. β-energy curves projected to positive-parity. In smaller and larger β regions, oblate and prolate shapes are obtained, respectively. (See text)

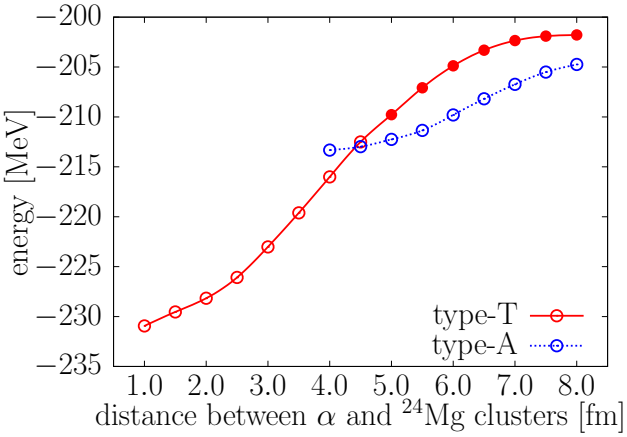

Fig. 2. $d_{\alpha\text{-}^{24}\mathrm{Mg}}$-energy curves projected to positive-parity states. Filled circles are obtained by hand. (See text)

case of d-constrained wave functions, the z-axis is chosen as the vector $\mathbf{R}_{\mathrm{C}_m\text{-}\mathrm{C}_n}$, which connects the C_m and C_n clusters. The coefficients f_{iK}^{β} and $f_{iK}^{d_{\mathrm{C}_m\text{-}\mathrm{C}_n}}$ are determined by the Hill-Wheeler equation,

$$\delta\left(\langle\Phi_M^{J^\pi}|\hat{H}|\Phi_M^{J^\pi}\rangle - \epsilon\langle\Phi_M^{J^\pi}|\Phi_M^{J^\pi}\rangle\right) = 0. \qquad (16)$$

Then we get the energy spectra and the corresponding wave functions that expressed by the superposition of the optimum wave functions, $\{|\Phi_i^{\beta}\rangle\}$, $\{|\Phi_i^{d_{\alpha\text{-}^{24}\mathrm{Mg}}}\rangle\}$, and $\{|\Phi_i^{d_{^{12}\mathrm{C}\text{-}^{16}\mathrm{O}}}\rangle\}$.

3 Structures obtained by constrained energy variation

By energy variation under the constraints on quadrupole deformation parameter β and inter-cluster distance $d_{\alpha\text{-}^{24}\mathrm{Mg}}$ and $d_{^{12}\mathrm{C}\text{-}^{16}\mathrm{O}}$ for α-^{24}Mg and ^{12}C-^{16}O cluster structures, respectively, energy curves as functions of β, $d_{\alpha\text{-}^{24}\mathrm{Mg}}$ and $d_{^{12}\mathrm{C}\text{-}^{16}\mathrm{O}}$ are obtained. On the curves, various structures appear.

Figure 1 shows the β-energy curves for the positive-parity states before and after the angular momentum projection to $J^\pi = 0^+$ states. The obtained wave functions always have axially symmetric shapes, though the mass quadrupole deformation parameter γ for triaxiality is not constrained and optimized by the energy variation. In the small deformed region $\beta \lesssim 0.5$, the system is oblately deformed and the surface has a shallow minimum. In the large deformed region $\beta \gtrsim 0.4$, the system has prolate deformation and two local minima around $\beta = 0.5$ and 0.7 that we call ND and SD minima in the following discussion.

We next discuss the results obtained by energy variation while imposing the d constraint. Figure 2 shows the energy curve obtained by the $d_{\alpha\text{-}^{24}\mathrm{Mg}}$ constraint. The energies of the positive-parity states are shown as functions of the inter-cluster distance. Two types of shapes are obtained by energy variation. One is the triaxial shape (denoted as type-T) and the other is the axial symmetric shape (denoted as type-A). The ^{24}Mg cluster in the α-^{24}Mg cluster structures deforms prolately. In case of type-A, the α cluster is located on the symmetric axis of the deformed ^{24}Mg cluster, while in the case of type-T, the orientation of the deformed ^{24}Mg cluster is transverse and the longitudinal axis of the ^{24}Mg cluster is perpendicular to the inter-cluster direction. The type-T wave functions are obtained in small $d_{\alpha\text{-}^{24}\mathrm{Mg}}$ region. With the increase of $d_{\alpha\text{-}^{24}\mathrm{Mg}}$, the structure changes from the type-T into the type-A structure. As mentioned above, in the large $d_{\alpha\text{-}^{24}\mathrm{Mg}}$ region, the type-A wave function is favored and the type-T wave functions are not obtained by the energy variation. As shown later, the obtained type-T wave functions are found to play an important role for an α-cluster band. To check the behavior of the type-T structure in the large $d_{\alpha\text{-}^{24}\mathrm{Mg}}$ region and its effect on the band structure, we have prepared the type-T wave functions with $d_{\alpha\text{-}^{24}\mathrm{Mg}} = 5.0 - 8.0$ fm by shifting by hand the α cluster position in the type-T wave function at $d_{\alpha\text{-}^{24}\mathrm{Mg}} = 4.5$ fm (filled circles in Fig. 2).

4 Band structures

4.1 MCM calculation and energy levels

We have performed the MCM calculation by using the obtained basis wave functions. The adopted basis are 22 β-constrained with $\beta = 0.07$–0.48 for oblate shapes and $\beta = 0.37$–0.95 for prolate shapes, 15 type-T and nine type-A $d_{\alpha\text{-}^{24}\mathrm{Mg}}$-constrained wave functions with $d_{\alpha\text{-}^{24}\mathrm{Mg}} = 1.0$–$8.0$ fm and 4.0–8.0 fm, respectively, and six type-T and six type-A $d_{^{12}\mathrm{C}\text{-}^{16}\mathrm{O}}$-constrained wave functions with $d_{^{12}\mathrm{C}\text{-}^{16}\mathrm{O}} = 5.5$–$8.0$ fm and $d_{^{12}\mathrm{C}\text{-}^{16}\mathrm{O}} = 3.5$–$6.0$ fm, respectively. In the MCM calculation, $|K| \leq 2$ and $\langle\Phi|\hat{P}_{KK}^{J^\pi}|\Phi\rangle/\langle\Phi|\Phi\rangle > 0.005$ states are adopted as the MCM basis. Other states are omitted, because they contain numerical errors in the numerical integration of the angular momentum projection. The convergence of the MCM calculation is confirmed by changing the number of the basis wave functions.

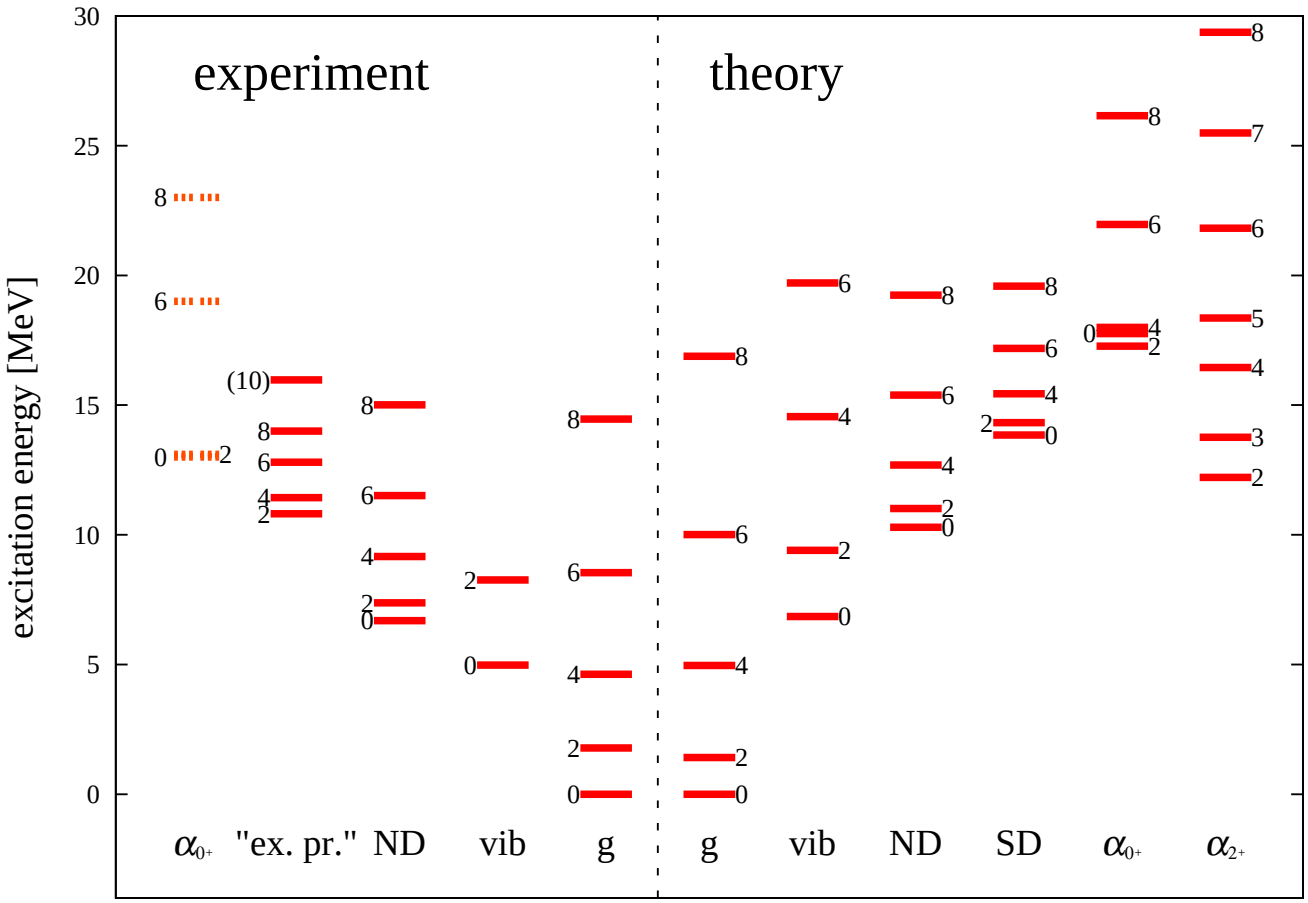

Fig. 3. Level scheme of positive-parity states in ^{28}Si is shown. Left and right panels are for experimental and theoretical values, respectively. The experimental data are taken from Refs. [12] and [22]. The "ex. pr." indicates "excited prolate" band.

As shown in the energy spectra in Fig. 3, many rotational bands are constructed due to the coexistence of various structures. An oblate ground (g) band, a β vibration (vib) band, a ND band and a SD band are obtained. Moreover, two α cluster bands (α_{2^+} and α_{0^+}) with α-^{24}Mg cluster structure are found in high excited states. As for the experimental α_{0^+} band, averaged values of the excitation energy are listed because those states are fragmented (dotted lines)[14].

4.2 Shape coexistence and β vibration

The excitation energies of the ground state band and β vibration band members have good agreement with experimental data. As for the ND band, the calculated excitation energies are slightly higher than the experimental ones, but the calculations reproduce well the level spacing in the ND band as shown in Fig. 4, which shows moments of inertia as functions of angular momentum. That is, both theoretical and experimental values of moments of inertia of the ND band are almost constant and approximately 4 $\hbar^2$/MeV.

To analyze the wave functions of the ground, β vibration, ND, and SD bands, squared overlaps $S_{\beta=\beta_i} = |\langle \Phi^{\rm MCM}|\Phi^{\beta}_i\rangle|^2$ with β-constrained wave functions are used,

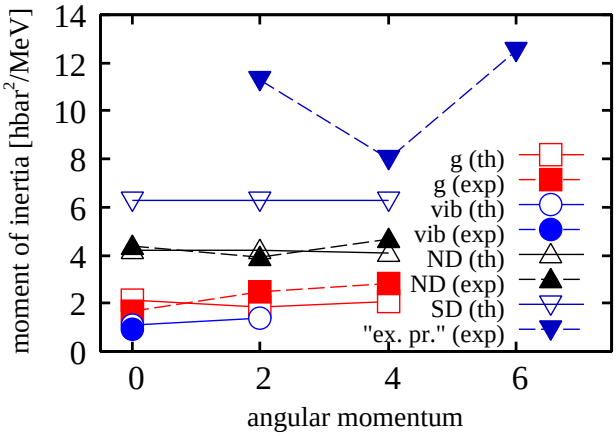

Fig. 4. Moments of inertia for the ground, β vibration, ND and SD band. Open and closed symbols indicate theoretical and experimental values, respectively. The definition of moment of inertia is $\mathcal{J}(J) = \frac{2J+3}{E(J+2)-E(J)}\hbar^2$, where $E(J)$ is excitation energy of the angular momentum J state.

as shown in Fig. 5, where the β_i is the value of the quadrupole deformation parameter β for the $|\Phi^{\beta}_i\rangle$. The

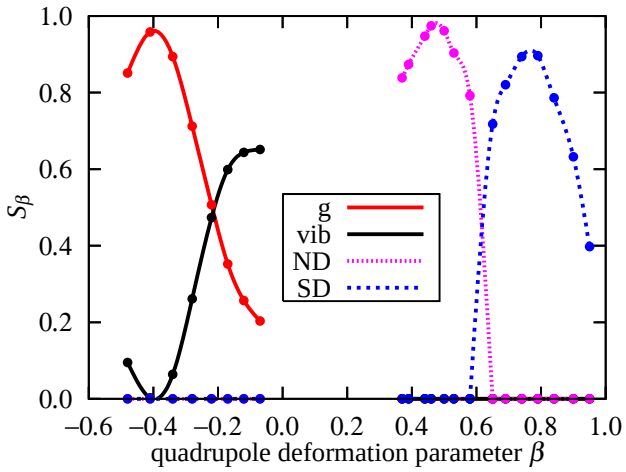

Fig. 5. Squared overlaps with β-constrained wave functions as functions of quadrupole deformation parameter β for ground, β vibration, ND, and SD bands are shown. β values are defined as negative values for oblate shapes.

$S_{\beta=\beta_i}$ values for the band-head 0^+ states are plotted as functions of quadrupole deformation parameter β. The wave functions of both the ground and β vibration bands have large amplitudes in the oblate region, and it is found that the $J^\pi = 0^+_{\rm vib}$ state appears due to its orthogonality to the ground state $J^\pi = 0^+_{\rm gs}$, which shows a β vibration mode. The ground state band amplitudes a peak at $\beta = -0.4$, which shows a rather large deformation. The ND and SD bands have large amplitudes at prolate regions ($\beta \simeq 0.4$ and 0.8, respectively). These results suggest the shape coexistence of the oblate and prolate normal-deformations and the prolate superdeformation.

4.3 Superdeformed band

The present result predicts the SD band starting form $J^\pi = 0^+$ state at 13.8 MeV, though the SD band has not been clearly identified. There are experimental works that argue for the existence of the "excited prolate" band with a large moment of inertia starting from the state at around 10 MeV[12, 11, 13]. We compare the theoretical SD band and the experimental "excited prolate" band.

As shown in Figs. 1 and 5, SD states are obtained by wave functions around the local minimum at $\beta \simeq 0.8$. Reflecting the large deformation, the moments of inertia are large, and take a value of approximately 6 $\hbar^2$/MeV as shown in Fig. 4. However, the moments of inertia for the "excited prolate" band deduced from the band assignment of the experimental work are much larger than those of the theoretical SD band. The present results unsupport the band assignment of "excited prolate" band. To conclude the correspondence of the theoretical SD band and the "excited prolate" band, more experimental information, such as intra-band transitions, are required. As shown in the next subsection, large strengths for the electric quadrupole transition are suggested in the present SD band.

Table 1. Electric quadrupole transition strengths $B(E2)$ are shown. Units are in Weisskopf unit $B(E2)_{\rm W.u.} = 5.05e^2{\rm fm}^4$ for ^{28}Si. J_i and J_f are the angular momentum of initial and final states, respectively. Experimental data are also listed. The experimental data are taken from Ref. [22].

J_i	J_f	experiment	theory
$2^+_{\rm gs}$	$0^+_{\rm gs}$	13.2 ± 0.3	15.0
$4^+_{\rm gs}$	$2^+_{\rm gs}$	13.8 ± 1.3	23.2
$6^+_{\rm gs}$	$4^+_{\rm gs}$	9.9 ± 2.5	28.6
$2^+_{\rm vib}$	$0^+_{\rm vib}$	5.5 ± 1.3	8.7
$2^+_{\rm ND}$	$0^+_{\rm ND}$	—	41.7
$4^+_{\rm ND}$	$2^+_{\rm ND}$	29 ± 5	57.4
$6^+_{\rm ND}$	$4^+_{\rm ND}$	> 16	59.1
$2^+_{\rm SD}$	$0^+_{\rm SD}$	—	132.1
$4^+_{\rm SD}$	$2^+_{\rm SD}$	—	188.1
$6^+_{\rm SD}$	$4^+_{\rm SD}$	—	205.8

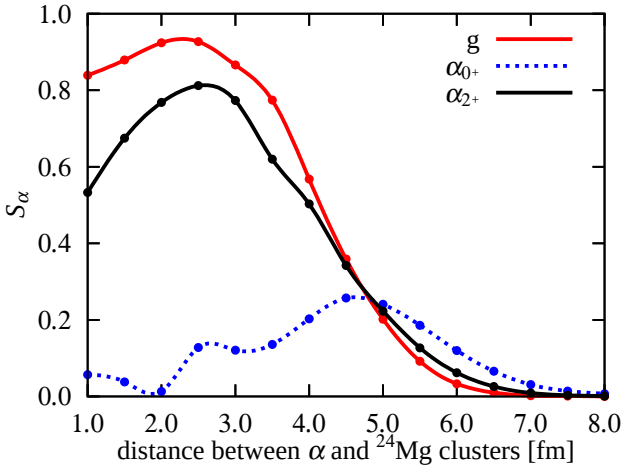

Fig. 6. α-^{24}Mg cluster structure component S_α of the $J^\pi = 2^+$ states in the gs, α_{0^+} and α_{2^+} bands as functions of distance between α and ^{24}Mg clusters.

4.4 Electric quadrupole transition strengths $B(E2)$

Table 1 shows electric quadrupole transition strengths $B(E2)$ of intra- and inter-band transitions. Experimental data are also listed.

Reflecting the large deformation of the ND and SD states, the $B(E2)$ values for their intra-band transitions are large. Compared to the experimental data, the $B(E2)$ values are overestimated. Especially, $B(E2; 6^+_{\rm gs} \rightarrow 4^+_{\rm gs})$ is much overestimated. It might be because structural changes with an increase of angular momentum are not represented enough in the present framework, which uses variation before angular momentum projection.

5 Cluster correlations

Figure 6 shows the type-T α-^{24}Mg cluster structure component S_α of the $J^\pi = 2^+$ states in the ground, α_{0^+} and α_{2^+} bands as functions of the distance $d_{\alpha\text{-}^{24}{\rm Mg}}$. As shown in

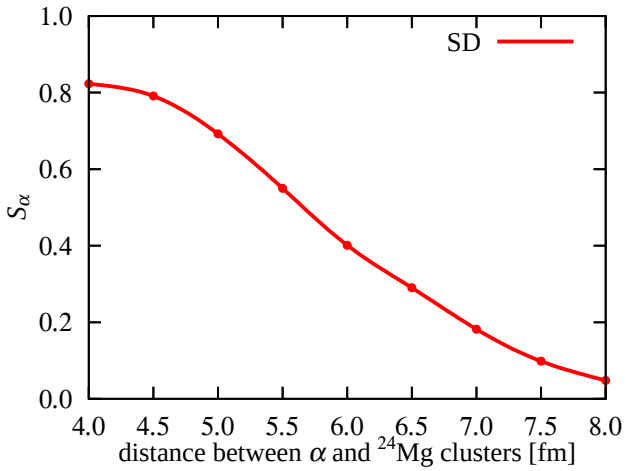

Fig. 7. α-^{24}Mg cluster structure component S_α of the $J^\pi = 2^+$ states in the SD bands as functions of distance between α and ^{24}Mg clusters.

the figure, the amplitudes for the $J^\pi = 2^+_{\rm gs}$ in the ground state band are concentrated in the small $d_{\alpha\text{-}^{24}{\rm Mg}}$ region, while those for the $J^\pi = 2^+_{\alpha_{0^+}}$ states are compressed in the small distance region compared to the ground state band, and they have a peak at $d_{\alpha\text{-}^{24}{\rm Mg}} \sim 5$ fm. This figure shows the typical α-^{24}Mg higher-nodal nature of the α_{0^+} band built on the ground state band due to the excitation of inter-cluster motion. As mentioned before, the candidates for the members of the α-cluster band have been observed by ^{24}Mg(^{6}Li, d) and ^{24}Mg(α, α) reactions. The observed $K^\pi = 0^+$ band may correspond to the α_{0^+} band though the excitation energies are slightly overestimated by the present calculations.

As for the α_{2^+} band, the $J^\pi = 2_{\alpha_{2^+}}$ state shows a large amplitude of S_α in the small $d_{\alpha\text{-}^{24}{\rm Mg}}$ region, similar to the $J^\pi = 2^+_{\rm gs}$ in the ground state band. It shows that the α_{2^+} band is regarded as a counter part of the ground state band due to the K-mixing because of the triaxial deformation of the type-T α-^{24}Mg cluster structure. In particular, the α_{2^+} band has a $|K| = 2$ feature of the type-T α-^{24}Mg cluster structure. Here, the K is defined with respect to the z-axis set to the inter-cluster direction of the α and ^{24}Mg clusters, and the orientation of the prolate ^{24}Mg cluster is perpendicular to the z-axis as mentioned before. Therefore, the α_{2^+} band is interpreted as the α-^{24}Mg cluster band with the cluster core excitation of ^{24}Mg(2^+). On the experimental side, there is no established band with $K^\pi = 2^+$. To search for the α_{2^+} band, observation of unnatural parity states might be helpful.

The SD band members contain a large $\alpha_{\rm A}$ component. Therefore, the SD states are expected to be observed in α-transfer reactions. It should be noted that the SD state contains only the component of the type-A α-^{24}Mg structure that has the very longitudinal structure. This property is in contrast to the case of the ground state band which contains only the type-T α-^{24}Mg component.

6 Conclusions

Positive-parity states in ^{28}Si have been studied using the deformed-basis AMD + MCM focusing on clustering and deformation. The experimental energy levels in the low-energy region are reproduced well by the present calculations. The oblately deformed ground state band and prolately deformed excited band are reproduced, and the result shows shape coexistence. The β vibration band also appears because the oblately deformed state is soft against quadrupole deformation. A superdeformed band is suggested in the present results. If the suggested SD band of ^{28}Si is observed experimentally it should be the superdeformation of the lightest *sd*-shell nucleus. Existence of largely deformed band ("excited prolate") has been proposed experimentally, but we cannot assign the experimental band with the theoretical SD band because the experimental moment of inertia is not consistent with that of the calculated SD band. More experimental data such as electric or magnetic transitions are requested.

The cluster bands, α_{0^+} and α_{2^+} bands also have been obtained. These bands contain significant α-^{24}Mg cluster structure components. The α_{0^+} band is regarded as the higher-nodal band due to the excitation of inter-cluster motion, while the α_{2^+} band is interpreted as the $K^\pi = 2^+$ band due to the triaxiality of the α-^{24}Mg cluster structure.

It is found that cluster components are significantly contained in the low-lying deformed states as well as the cluster bands. Namely, the gs and SD bands contain a significant α-^{24}Mg cluster structure component. Those results are analogous to situations of other *sd*-shell nuclei such as ^{32}S for which ^{16}O-^{16}O correlations in the SD band have been suggested[5,23], and ^{40}Ca where α-^{36}Ar correlations in the ND band and ^{12}C-^{28}Si correlations in the SD band have been discussed[3,6].

We have shown the importance of clustering effects as well as deformation effects in low-lying states of ^{28}Si. That finding is consistent with the recent full-microscopic studies that suggested that both clustering and deformations play important roles in the wide-range *sd*-shell region.

Acknowledgements

The authors would like to thank Dr. M. Takashina for fruitful discussions. The numerical calculations have been carried out on SX8 at YITP, Kyoto University, SX8R at RCNP, Osaka University, and supercomputers at KEK. This work has been partly supported by the Grant-in-Aid for Scientific Research from JSPS, and the Grant-in-Aid for the Global COE Program "The Next Generation of Physics, Spun from Universality and Emergence" from MEXT of Japan.

References

1. H. Horiuchi, K. Ikeda, Y. Suzuki, Prog. Theor. Phys. Suppl. **52**, 89 (1972), and references therein

2. Y. Fujiwara, H. Horiuchi, K. Ikeda, M. Kamimura, K. Katō, Y. Suzuki, E. Uegaki, Prog. Theor. Phys. Suppl. **68**, 29 (1980), and references therein
3. Y. Taniguchi, M. Kimura, Y. Kanada-En'yo, H. Horiuchi, Phys. Rev. C **76**, 044317 (2007)
4. M. Kimura, H. Horiuchi, Nucl. Phys. A **767**, 58 (2006)
5. M. Kimura, H. Horiuchi, Phys. Rev. C **69**, 051304 (2004)
6. Y. Kanada-En'yo, M. Kimura, Phys. Rev. C **72**, 064322 (2005)
7. F. Glatz, J. Siefert, P. Betz, E. Bitterwolf, A. Burkard, F. Heidinger, T. Kern, R. Lehmann, S. Norbert, H. Röpke, Z. Phys. A **303**, 239 (1981)
8. F. Glatz, P. Betz, J. Siefert, F. Heidinger, H. Röpke, Phys. Rev. Lett. **46**, 1559 (1981)
9. R.K. Sheline, S. Kubono, K. Morita, M.H. Tanaka, Phys. Lett. B **119**, 263 (1982)
10. S.D. Gupta, M. Harvey, Nucl. Phys. A **94**, 602 (1967)
11. S. Kubono, K. Morita, M.H. Tanaka, A. Sakaguchi, M. Sugitani, S. Kato, Phys. Rev. C **33**, 1524 (1986)
12. S. Kubono, K. Morita, M.H. Tanaka, A. Sakaguchi, M. Sugitani, S. Kato, Nucl. Phys. A **457**, 461 (1986)
13. S. Kubono, M.H. Tanaka, S. Kato, M. Yasue, M. Sekiguchi, H. Kamitsubo, T. Tachikawa, Phys. Lett. B **103**, 320 (1981)
14. K.P. Artemov, M.S. Golovkov, V.Z. Goldberg, V.I. Dukhanov, I.B. Mazurov, V.V. Pankratov, V.V. Paramonov, V.P. Rudakov, I.N. Serikov, V.A. Solovev et al., Sov. J. Nucl. Phys. **51**, 777 (1990)
15. J. Cseh, E. Koltay, Z. Máté, E. Somorjai, L. Zolnai, Nucl. Phys. A **385**, 43 (1982)
16. Y. Taniguchi, Y. Kanada-En'yo, M. Kimura, Phys. Rev. C **80**, 044316 (2009)
17. M. Kimura, Phys. Rev. C **69**, 044319 (2004)
18. Y. Taniguchi, M. Kimura, H. Horiuchi, Prog. Theor. Phys. 112, **475** (2004)
19. A. Doté, H. Horiuchi, Y. Kanada-En'yo, Phys. Rev. C **56**, 1844 (1997)
20. J. Berger, M. Girod, D. Gogny, Comp. Phys. Comm. **63**, 365 (1991)
21. Y. Kanada-En'yo, H. Horiuchi, Prog. Theor. Phys. **93**, 115 (1995)
22. P.M. Endt, Nucl. Phys. A **633**, 1 (1998)
23. S. Ohkubo, K. Yamashita, Phys. Rev. C **66**, 021301 (2002)